Design Recommendations for Single and Dual Debris Flow Barriers with and Without Basal Clearance

Charles Wang Wai Ng, Clarence Edward Choi, Haiming Liu, Sunil Poudyal, and Julian Shun Hang Kwan

Abstract

Debris flows pose threats to sustainable development in many countries worldwide, including China, Japan, Switzerland and USA. To mitigate these flows, rigid and flexible barriers are commonly installed along the predicted flow paths. To arrest large volumes of debris flow, several barriers may be installed in series to create a cascading effect to progressively decelerate and retain the debris. Barriers may even be designed with a basal clearance to allow small discharges to pass underneath the barrier to reduce the peak impact force. Despite the importance of barriers as life-saving assets, their design remains essentially empirical because of the highly heterogeneous and scale-dependent nature of debris flow. These features of debris flow have hindered an understanding of their fundamental impact mechanisms, thereby hampering the development of scientific design guidelines to enable robust and cost-effective barriers. This forum paper presents a collection of physical experiments modelling the impact mechanisms of the two extreme cases of water and dry granular flows, and two-phase debris flows against single and dual rigid barriers, and a single flexible barrier. Furthermore, the effects of a basal clearance on the impact dynamics of dry granular flow against a single rigid barrier are examined. Experiments were conducted at two different scales, including 5 m-long and 28 m-long flumes. Based on the observed impact mechanisms and measured data, a newly developed analytical framework for designing multiple rigid barriers was evaluated. Recommendations and procedures are provided for the design of single and multiple rigid barriers with and without a basal clearance.

Keywords

Debris flow • Impact • Rigid barrier • Flexible barrier • Multiple barriers • Physical modelling • Basal clearance

Introduction

Debris flows, which are mixtures of soil and water, surge down mountainsides under the influence of gravity at high velocities. Such flows often result in fatalities (Froude and Petley 2018) and damage to infrastructure (Jakob et al. 2012). To arrest these flows, a single large reinforced concrete rigid barrier (Fig. 1) is conventionally constructed at the end of a catchment. Such an approach may enable a debris flow to increase in velocity and volume via entrainment (Berger et al. 2011) before impacting the barrier. Consequently, a larger barrier with a higher design capacity is required. With the challenges of land scarcity in densely populated urban areas, such as Hong Kong, and the importance of preserving the natural environment, bulky reinforced concrete barriers are decreasingly viable in terms of sustainability. Given these challenges, smaller rigid barriers in series along a channel provide an ideal solution to create a cascading effect to dissipate flow energy and reduce the flow volume. However, there are no design guidelines on how to space barriers in series to optimise their design loads.

C. W. W. Ng · H. Liu · S. Poudyal
Department of Civil and Environmental Engineering, The Hong Kong University of Science and Technology, Hong Kong SAR, China
e-mail: cecwwng@ust.hk

H. Liu
e-mail: hliubc@connect.ust.hk

S. Poudyal
e-mail: spoudyal@connect.ust.hk

C. E. Choi (✉)
Department of Civil Engineering, The University of Hong Kong, Hong Kong SAR, China
e-mail: cechoi@hku.hk

J. S. H. Kwan
Civil Engineering and Development Department, Geotechnical Engineering Office, Hong Kong SAR, China
e-mail: juliankwan@cedd.gov.hk

© Springer Nature Switzerland AG 2021
K. Sassa et al. (eds.), *Understanding and Reducing Landslide Disaster Risk*,
ICL Contribution to Landslide Disaster Risk Reduction,
https://doi.org/10.1007/978-3-030-60196-6_2

Another important design feature of rigid barriers is the basal clearance (Fig. 2), which is an opening at the base of a barrier (Piton and Recking 2015). These clearances are often included to prevent smaller discharges from being trapped, which over time depletes the design retention capacity intended for larger and more dangerous debris flow events. The basal clearance also regulates the volume of retained debris and allows discharge underneath the barrier. Sze and Lam (2017) summarised international guidelines and reported that basal clearances of up to 1.5 m are commonly used in barrier designs. However, it is evident from their report that the sizing of a basal clearance is essentially empirical. Without a scientific basis for design, basal clearances that are too large render a barrier ineffective at reducing the peak impact load, while clearances that are too small give rise to uncontrolled overflow and increase the impact and drag loads induced on a barrier. Evidently, research is required to shed light on an optimum basal clearance.

Aside from rigid barriers, flexible barriers have become an emerging structural countermeasure in debris flow hazard mitigation. Over the past decade, flexible barriers for rock fall have been impacted by debris flow and proved to be effective at arresting debris flows. However, the impact dynamics of a rock fall and debris flow are fundamentally different. Therefore, the design of flexible barriers for debris flows remains largely empirical. Compared with reinforced concrete rigid barriers, flexible barriers (Fig. 3) blend in well with their natural surroundings and are easy to install. More importantly, the deformation of flexible barriers is ideal for attenuating impact forces (DeNatale et al. 1999; Wendeler et al. 2006; Brighenti et al. 2013; Ng et al. 2016). To use flexible barriers more extensively in mountainous regions, research is required to elucidate the fundamental impact mechanisms so that design guidelines can be developed.

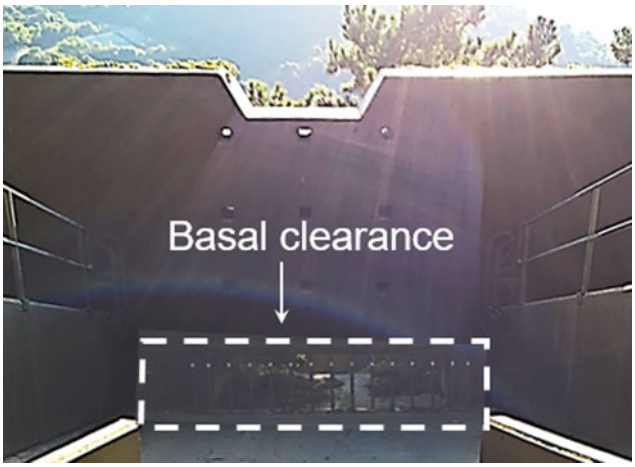

Fig. 2 Basal clearance under a rigid barrier (Tung Chung, Hong Kong)

In existing international design guidelines (Kwan 2012; Volkwein 2014), the impact force exerted by a debris flow is calculated as follows:

$$F = \alpha \rho v^2 h_0 w \tag{1}$$

where α is a dynamic impact coefficient; ρ is the flow density; v is the velocity of the flow; h_0 is the flow depth and w is the channel width. To ensure robust design loads, international guidelines (Lo 2000; ASI 2008) often prescribe high α values to account for the idiosyncrasies involved in natural materials and settings in the field. For instance, Kwan (2012) recommends an α of 2.5 for the design of rigid reinforced concrete barriers and an α of 2.0 for flexible barriers. These recommended values account for hard inclusions in the flow. Figure 4 shows a typical impact load

Fig. 1 Rigid barrier (Cheung Tung Road, Hong Kong) (DB 2020)

Fig. 3 Flexible barrier (Hiroshima, Japan)

model for the design of rigid barriers against debris flow impact in Hong Kong. In their guidelines, they generally recommend that each surge impacting a barrier should be designed using the maximum velocity and flow depth obtained from a debris mobility analysis (Kwan and Koo 2015). However, Koo et al. (2017) reported that these assumptions were over-conservative, and recommended a velocity attenuation model. Nevertheless, there is room to improve the estimation of design impact loads and optimise the design of barriers.

Further compounding the challenges in designing barriers is dealing with the scale-dependency and heterogeneous nature of debris flow. Iverson (2015) reported that small-scale two-phase debris flow models cannot replicate the timescales for pore pressure dissipation and the ratio between viscous and inertial stresses observed in field events. Therefore, unique physical modelling facilities are necessary to replicate the appropriate debris flow dynamics. Furthermore, the characteristics of debris flows are catchment specific (Rickenmann 1999), some flows may be more frictional, while some may be more viscous. Choi et al. (2015) reported that frictional and viscous flows exhibit entirely different impact mechanisms. Frictional flows exhibit a pileup mechanism (Koo et al. 2017), while viscous flows exhibit a vertical jet mechanism (Ng et al. 2019). One can imagine that complex two-phase debris flows must exhibit some characteristics of the two idealised flows. Without a clear understanding of these fundamental impact mechanisms, it remains unclear whether Eq. 1 is over-conservative, adequate or unsafe.

In this forum paper, physical experiments that model the complex impact mechanisms of dry granular, water, and two-phase debris flows on single and dual rigid barriers and a single flexible barrier are presented. In addition, the effects of a basal clearance on a single rigid barrier are examined. Experiments were conducted at two different scales, including 5 m-long and 28 m-long flumes. Based on the observed fundamental impact mechanisms, an analytical framework for designing multiple rigid barriers was developed and then evaluated using experimental data. Finally, recommendations are provided for the design impact load for single rigid barriers with and without a basal clearance, a dual rigid barrier system, and a single flexible barrier.

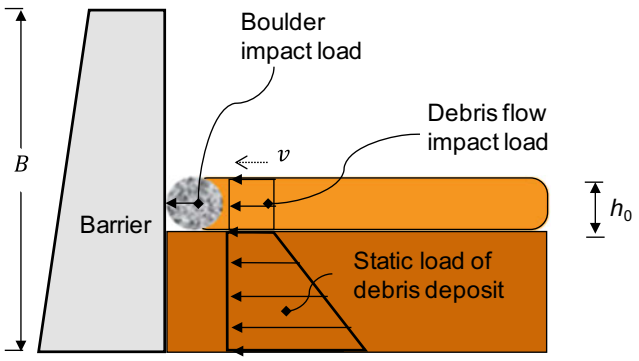

Fig. 4 Impact model proposed by Kwan (2012)

Analytical Framework for Dual Rigid Barriers

Conventionally, the design of multiple barriers in series is based on the estimated retention of the total debris volume (NILIM 2007; Faug et al. 2012). More recently, the impact dynamics between debris flows and barriers in series have been reported as important considerations in design (Kwan et al. 2015; Ng et al. 2018). Figure 5 shows a newly proposed analytical framework for multiple rigid barriers in series (Kwan et al. 2015). This framework includes a set of velocity-attenuation and impact equations for rigid barriers that captures the dissipation of kinetic energy as granular material is deposited in layers up to the crest of a barrier (Koo et al. 2017). The overflow then follows the trajectory of an inviscid jet from the barrier crest before landing on the channel bed. After landing on the channel bed, energy is dissipated before the granular material flows towards the next barrier in the channel (Ng et al. 2018; 2019). Details of the analytical framework for designing multiple rigid barriers are discussed below.

Velocity Attenuation Impact Model

When a granular flow impacts a rigid barrier, the material is arrested at the base of the barrier. Granular material then progressively deposits to the crest of the barrier (Koo et al. 2017; Ng et al. 2019). Figure 6 shows a granular flow with velocity v and depth h_0 on a channel inclined at θ. As the granular flow climbs on the wedge of deposited granular material, shearing occurs along their interface. The attenuated velocity from shear between the incoming flow and dead zone v_d and its corresponding velocity attenuation factor R_d can be calculated as follows (Koo et al. 2017; Ng et al. 2019):

$$v_d = v(1 - R_d) \tag{2}$$

and,

$$R_d = 1 - \sqrt{1 - \frac{2g(h_d + L_T \tan\phi)}{v^2}} \tag{3}$$

where g is the acceleration due to Earth's gravity, ϕ is the friction angle, L_T is the length of the free surface of the arrested granular material and h_d is the height of the deposited granular material. Equations 2 and 3 are used

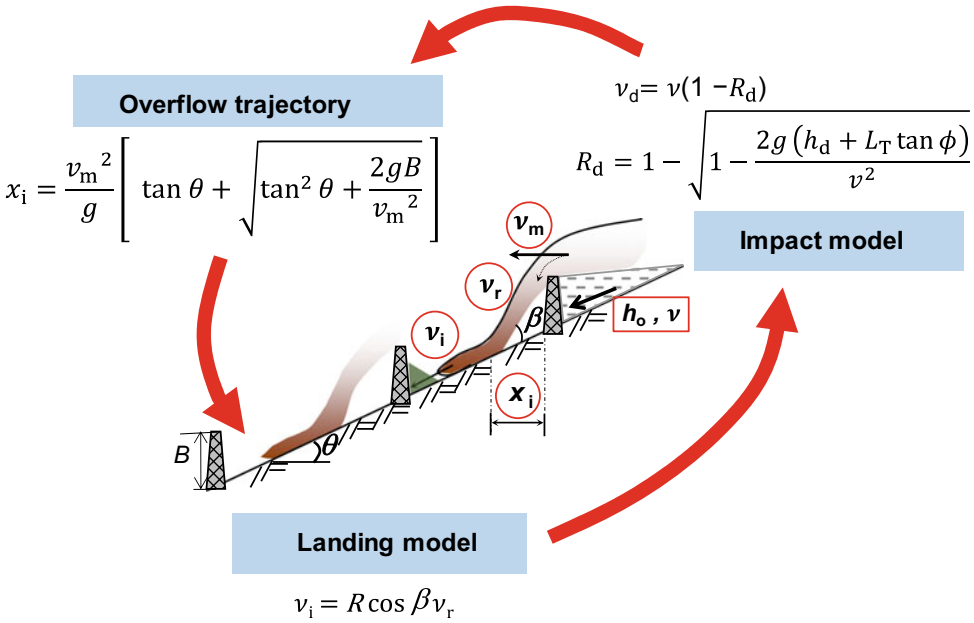

Fig. 5 Analytical multiple barrier framework (Kwan et al. 2015; Ng et al. 2018; Ng et al. 2019)

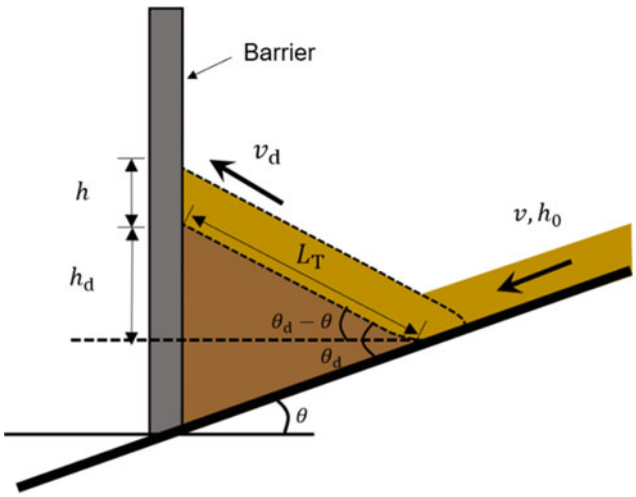

Fig. 6 A schematic diagram showing velocity attenuation mechanism (Koo et al. 2017)

repeatedly until the granular material has reached the crest of the barrier. The velocity attenuation model will be verified and discussed later.

Overflow Dynamics

Once the granular material reaches the crest of the barrier, overflow occurs. The overflowing material in the proposed framework is assumed to launch in the horizontal direction (Kwan et al. 2015). The overflow trajectory is then estimated by assuming a point mass as follows:

$$x_i = \frac{v_m^2}{g}\left[\tan\theta + \sqrt{\tan^2\theta + \frac{2gB}{v_m^2}}\right] \quad (4)$$

where v_m is the horizontal overflow velocity and B is the barrier height. The horizontal distance required to land on the channel x_i can then be used to determine the minimum spacing required between the barriers. Ideally, the overflow should be allowed to impact the channel bed before it is allowed to impact or overtop the next barrier in the channel to maximise the energy dissipated in the flow. In other words, the design spacing between barriers should be greater than x_i.

Landing

Energy is attenuated when overflow lands on the channel. Therefore, the flow velocity towards the next barrier v_i depends on the slope-parallel component of the landing velocity v_r and the angle of impact on the channel bed β. To account for changes in velocity after the overflowing debris impacts the channel bed, a landing coefficient C_r is introduced. The relationship between the velocity before and after landing is as follows:

$$v_i = C_r v_r \quad (5)$$

where $C_r = R\cos\beta$; R is the reduction factor of landing velocity due to friction between the flow and channel bed.

The attenuated velocity from Eq. (5) is then used as an input in Eqs. (2) and (3) to predict the impact dynamics on

the second barrier (Ng et al. 2019). Equations (2)–(5) can be repeatedly used to design the third and subsequent barriers installed downstream in the channel. Details about the verification of the analytical framework by physical experiment results are illustrated later.

Physical Modelling of Flow-Barrier Interaction

To investigate the impact dynamics of debris flows against rigid and flexible barriers, and to evaluate the analytical framework for dual barriers, a series of physical model tests were carried out. Dry granular and water flows were modelled using a 5 m-long flume model, and two-phase debris flows were modelled using a 28 m-long flume model. The collection of flume experiment model flows impacting single rigid barrier with and without a basal clearance, a single flexible barrier, and dual rigid barriers is presented. Details of the test setups, instrumentation, test plans, and modelling procedures are discussed below.

Five Metre-Long Flume Modelling

A 5 m-long flume with a rectangular cross-section that has a width of 0.2 m and a depth of 0.5 m was used to study the impact dynamics of dry granular and water flows impacting single and dual rigid barriers. A storage container with a volume of 0.06 m^3 is located at the upstream end of the flume to hold the debris material, which is retained behind a remote-controlled gate. The debris material in the 5 m-long flume was modelled as water or Toyoura sand with an average particle diameter of 0.3 mm. Figure 7 shows a typical side view of the 5 m-long flume and the instrumentation layout. Flow kinematics were captured using high-speed cameras (Mikrotron motionblitz EoSens mini2) mounted at the side of the flume. Images with a resolution of 1300 × 1600 pixels were captured at a sampling rate of 640 frames per second. Images were then analysed using Particle Image Velocimetry (PIV) (White et al. 2003) to obtain velocity fields. Laser displacement sensors (Wenglor YT44 MGV80) were used to measure the flow depth along the centreline of the flume. Instrumented model rigid barriers were assembled by sandwiching load cells (KYOWA LUX200N) between an acrylic force plate and an aluminium reaction frame mounted inside the flume.

For the experiments modelling dual rigid barriers without basal clearance (Ng et al. 2018), the height of the first barrier was varied from 100 mm to 260 mm. The height of the second barrier was 500 mm to ensure that overflow did not occur. The first barrier was located at an inclined distance of 800 mm from the gate. The inclined distance between barriers was 1000 mm. For the experiments of the single rigid barrier with a basal clearance (Choi et al. 2020), clearances of 0 mm, 15 mm and 30 mm were modelled. The basal clearance heights (H_c) are normalised by the maximum flow depth (h_o). The single barrier was installed at 1100 mm from the gate. Details of the model rigid barrier with a basal clearance are shown in Fig. 8. The experiments were designed to investigate the effects of normalised basal clearances H_c/h_o ranging from 0.3 to 1.0 on the impact dynamics. Three different Froude numbers, governed by the flume inclination, are modelled. Specifically, Froude numbers of 3.2, 4.5 and 5.3, which are obtained at flume inclinations of 15º, 25º, and 35º, respectively. A summary of the test plan using the 5 m-long flume for the dual rigid barriers and rigid barrier with a basal clearance is given in Tables 1 and 2, respectively.

In each 5 m-long flume test, the appropriate barrier configuration is installed in the flume, then the debris material is placed in the storage container. The flume is then inclined to the appropriate inclination angle. Finally, the gate is released, and the debris is allowed to discharge downslope and impact the various barrier configurations installed in the flume.

Twenty-Eight-Metre-Long Flume Modelling

A 28 m-long flume (Fig. 9) is used to conduct physical experiments to gain new insight on the impact mechanisms of two-phase debris flows against dual rigid barriers and a single flexible barrier. The flume has a uniform rectangular cross-section with a width of 2 m and a depth of 1 m. The side walls are transparent on one side of the flume to enable the impact kinematics to be captured during experiments.

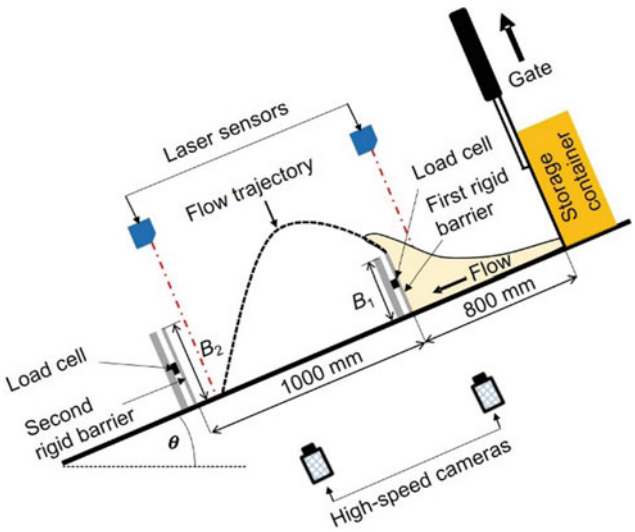

Fig. 7 A typical five-metre flume test setup with instrumentation of dual rigid barriers without basal clearance (not drawn to scale)

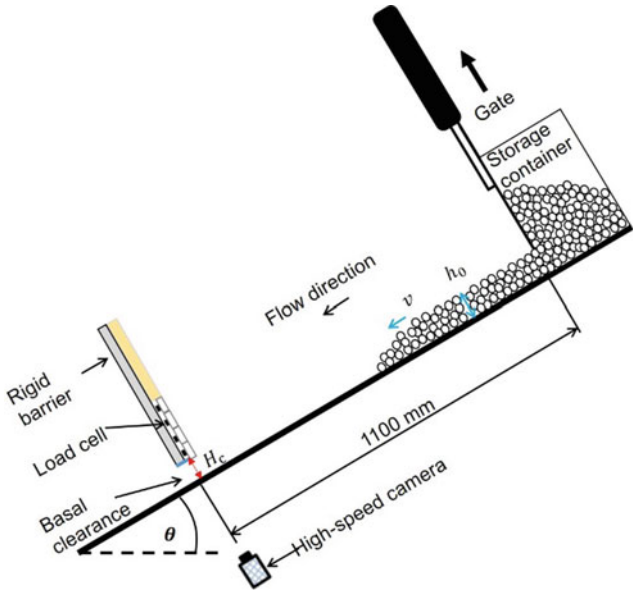

Fig. 8 A typical five-metre flume test setup with instrumentation of a single rigid barrier with basal clearance (not drawn to scale)

A storage container that can hold up to 10 m^3 is inclined at 30° at the top of the flume. The main flume is 15 m in length and has an inclination of 20°. The bottom part of the flume is horizontal and 8 m in length. A double gate system is used to retain debris material inside the storage container. The doors are secured and released using a mechanical arm, which is controlled by an electric motor. Laser and ultrasonic displacement sensors (Keyence IL600/IL1000 and Banner TUB30X) are mounted above the channel to measure the flow depth. Furthermore, high-speed cameras (Mikrotron EoSens 4CXP) are used in the 28 m-long flume tests to capture the impact kinematics and an unmanned aerial vehicle (DJI Phantom 3) is used to capture an aerial view of the experiment.

Dual rigid barriers (Fig. 10) are modelled to evaluate the multiple barrier framework for two-phase debris flows. The first barrier is a stiffened aluminium plate with a thickness of 20 mm, height of 500 mm and width of 2000 mm. Two steel supports at the flume sidewalls are used to fix the aluminium plate. A load cell is sandwiched between the support and the plate to measure the impact load. The second rigid barrier is a steel plate that is 1500 mm in height and 2000 mm in width. The steel plate is installed on a reinforced concrete structure. At each corner, a load cell is sandwiched between the steel plate and the reinforced concrete structure to measure the impact load. The first rigid barrier is installed at an inclined distance of 11 m from the gates and the second rigid barrier is installed at a curvilinear distance of 6 m from the first barrier.

A separate study was conducted to investigate the impact dynamics of debris flows on a flexible barrier. The flexible barrier has a ring net panel that is 2000 mm wide and 800 mm in height. The barrier is installed at an inclined distance of 13 m from the gate (Fig. 11). Each ring is 100 mm in diameter and made using steel wires that are 2 mm in diameter. The ring net panel is supported by two horizontal cables, which are anchored to the sidewalls of the flume. Tension load cells (TML TCLK50KNB) are used to measure the impact load of each cable. A mesh with 25 mm square openings made of 1 mm diameter stainless steel wire was overlaid onto the ring net to retain the debris material during and after impact. Dual spring elements (Ng et al. 2016; Fig. 12) are installed between ends of cable and anchors at flume side walls using eyebolts to replicate the loading response of an energy dissipating device used in prototype barriers. The dual spring element exhibits a bilinear load-displacement response. Each of the dual spring element comprises two compression springs—one stiff (k_1) and the other soft (k_2)—in series inside a cylinder. The springs are separated inside the cylinder by a coaxial separator. The flexible spring is preloaded to a specifiable load (P_{pre}) by adding a spacer between the spring and separator inside the cylinder. Before the applied load reaches the inflection point (P_{pre}), only the stiff spring resists the load and slope $K_1 = k_1$. After reaching the inflection point, the load is shared by both springs in series and the equivalent stiffness reduces to model the elongation of energy dissipating elements $K_2 = k_1 k_2/(k_1 + k_2)$. The peak deformation of dual spring elements is preserved by a pneumatic locking system.

In each 28 m-long flume experiment, the two-phase debris flow material is representative of the typical debris flow material in East Asia. This mixture generally comprises 35% gravel (20 mm), 62.5% sand (0.6 mm), and 2.5% clay (< 2 μm) (Ng et al. 2019). Figure 13 shows a textural classification of debris flow mixtures consisting of different percentages of gravel, sand and fines (silt and clay). A comparison was conducted between field mapping data from 50 debris flow events that occurred in June 2008 in Hong Kong (Sze and Lam 2017), relevant experiments (Bugnion et al. 2012; Iverson et al. 2010) and natural debris flows (Takahashi 1991; Remaitre et al. 2003; Choi 2010; Tecca et al. 2007). The majority of debris flows shown are predominantly sand-gravel mixtures, with limited samples of clay-rich debris. For Hong Kong cases, tests for particle size distribution were carried out using soil samples collected at debris deposition zone. Particles of size larger than 20 mm were not sampled. Mixtures with fine contents greater than 20% are classified as muddy flows (Bonnet-Staub 1999). A solid fraction of 0.6—typical in field debris flows (Iverson 2015)—is adopted for the testing material. The initial density of the mix is approximately 2,000 kg/m^3. This density lies within the range observed for natural debris flows, which typically ranges from 1,700 kg/m^3 to 2,400 kg/m^3 (Iverson

Table 1 Test programme for dual rigid barriers using the 5 m-long flume

Test ID	Material	Upstream barrier height (mm)	Downstream barrier height (mm)	Flume inclination (°)
WCI0	Water	Nil	Nil	0
WCI05				5
WCI10				10
WCI15				15
SCI26	Sand			26
SCI35				35
SCI45				45
WH10I0	Water	100	500	0
WH10I05				5
WH10I10				10
WH10I15				15
WH18I0		180		0
WH18I05				5
WH18I10				10
WH18I15				15
WH26I0		260		0
WH26I0				0
WH26I05				5
WH26I10				10
WH26I15				15
SH10I26	Sand	100		26
SH10I35				35
SH10I45				45
SH18I26		180		26
SH18I35				35
SH18I45				45
SH26I26		260		26
SH26I35				35
SH26I45				45

Table 2 Test programme for rigid barrier with basal clearance

Test ID	Basal clearance (mm)	Flume inclination (°)
C15-I15	15	15
C15-I25	15	25
C15-I35	15	35
C30-I15	30	15
C30-I25	30	25
C30-I35	30	35

and George 2014). It is worthwhile to note that hard and large inclusions were not explicitly modelled.

Before each 28 m-long flume experiment, the barriers were installed in the flume. The gates were then closed and the debris flow mixture was prepared in the storage container. After the debris mixture was ready, the gates were opened and debris was allowed to discharge downstream.

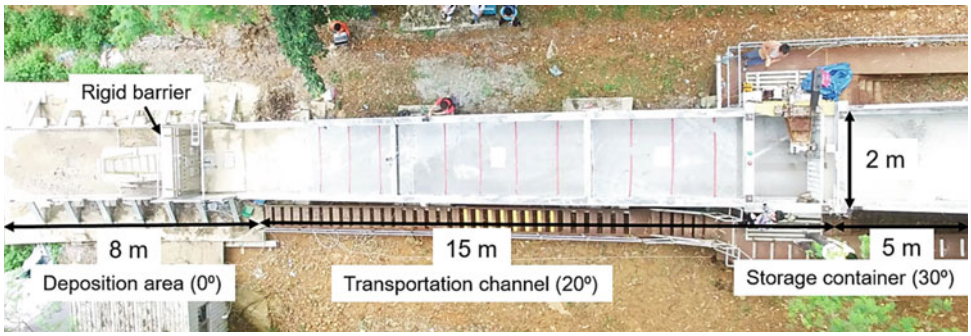

Fig. 9 Plan view of the 28 m-flume model

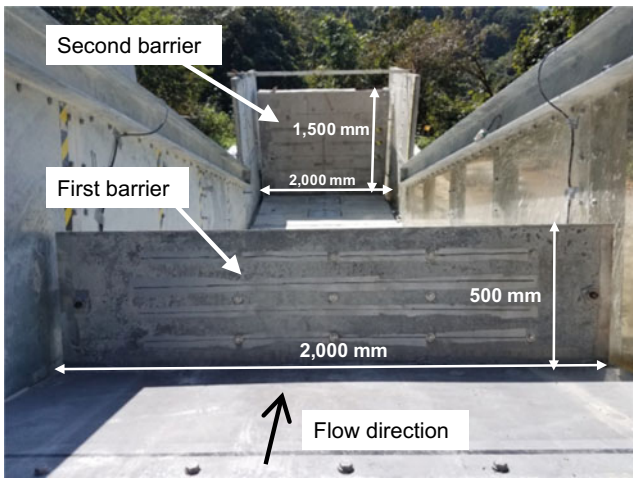

Fig. 10 Model dual rigid barriers

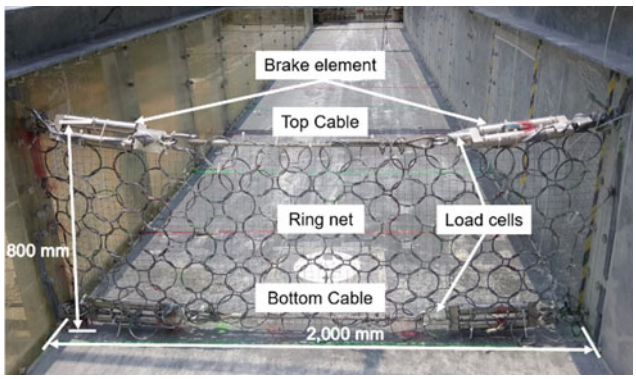

Fig. 11 Upstream view of model flexible barrier

Observed Impact Mechanisms

To develop impact models for design, the fundamental impact mechanisms must first be elucidated. This section examines the impact mechanisms of dry granular, water, and two-phase debris flows on rigid and flexible barriers using the 5 m-long flume and 28 m-long flume.

Single Rigid Barrier

Figure 14 shows a comparison of the impact kinematics of dry granular and water flows impacting against a single rigid barrier installed orthogonally to the channel bed. Tests were carried out in the 5 m-long flume. The flume is inclined at 26° and 5° for modelling dry granular and water flows, respectively. Figure 14a shows the kinematics of a dry granular flow impacting against a single rigid barrier. The kinematics, shown on the left, were captured using a high-speed camera and the corresponding velocity vectors from PIV analysis are shown on the right. At time t = 0 s, a tapered flow front reaches the barrier. Static deposits, called dead zone herein, accumulate at the base of the barrier and subsequent granular flow rides on top of the deposits. The granular flow then piles up along the face of the barrier (t = 0.50 s). The observed impact mechanism for dry granular flow on a rigid barrier is consistent with the layering mechanism proposed in the velocity attenuation model in Fig. 6. The granular material deposits in layers towards the crest of the barrier. As shearing occurs between the incoming flow and the deposited material forming the dead zone, the velocity of the incoming flow is attenuated. The attenuated flow eventually deposits and contributes to the dead zone. Velocity reduction is evident by examining the magnitude of the vectors deduced in the PIV analysis. The velocity reduces from 1.0 m/s to 0.5 m/s, which is a 50% decrease. At t = 1.00 s, the incoming flow is noticeably thinner due to a limited supply of granular material from the storage container. At t = 1.50 s, the barrier is filled to its crest. By using attenuated velocities to estimate the impact load using Eq. (1), lower impact loads can be obtained. The proposed velocity attenuation is implemented in design guidelines for rigid barriers in Hong Kong (Kwan and Koo 2015).

Figure 14b shows the kinematics of water flow impacting against a single rigid barrier (shown on the left), and the corresponding PIV analysis (shown on the right). The water flow front reaches the barrier at t = 0 s. The flow exhibits a

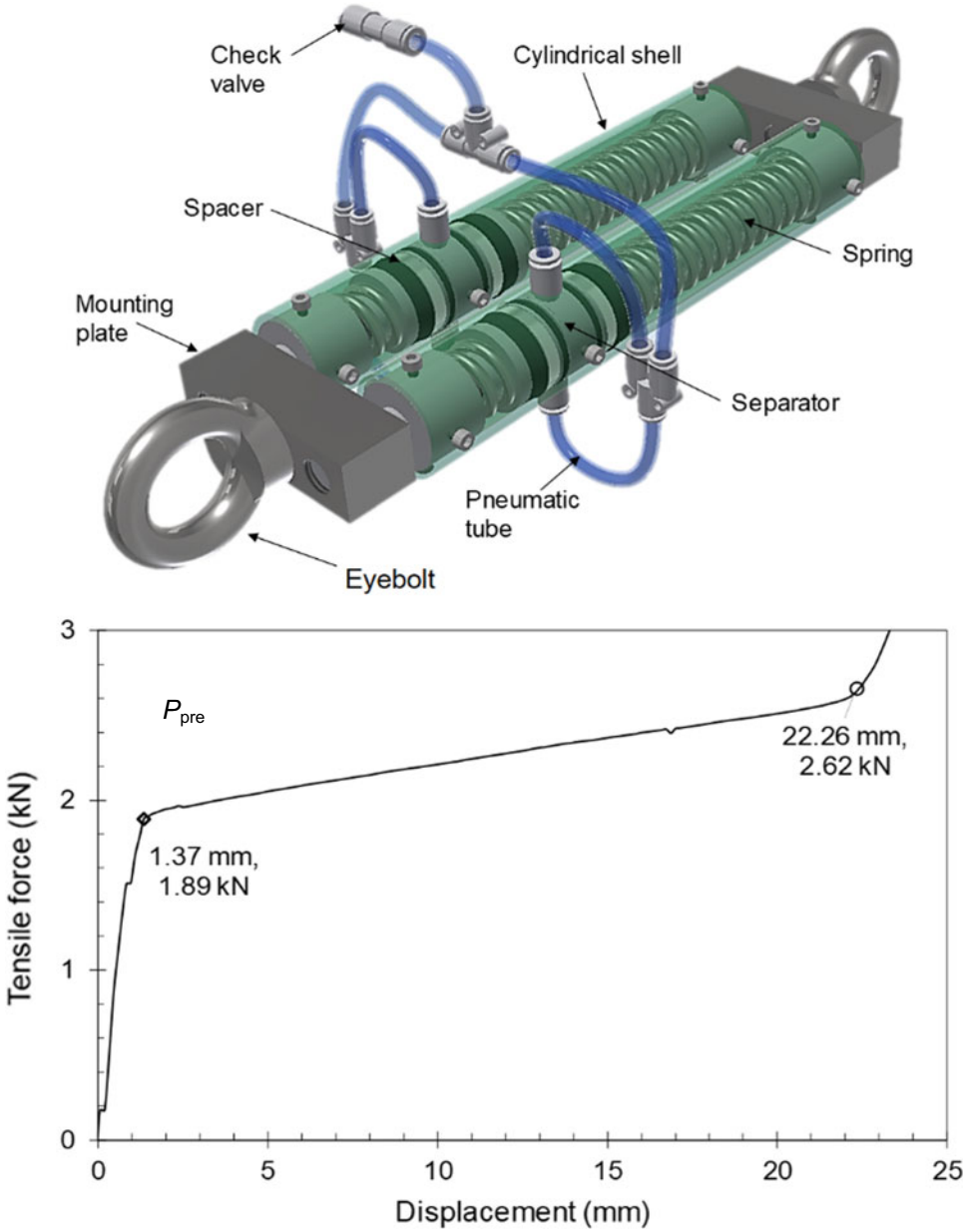

Fig. 12 Dual spring element model with force-displacement curve

vertical jet-like run-up (Choi et al. 2015) along the face of the rigid barrier upon impact at t = 0.15 s. The run-up height of the water exceeds the barrier height. The velocity vectors show a 90° redirection after impacting the barrier. At t = 0.5 s, the run-up rolls back towards the channel. Overspill is only observed at t = 1 s near the end of the impact process. Significant turbulence is observed as the water rolls-back and mixes with the incoming flow, further dissipating flow kinetic energy. Armanini et al. (2019) reported a similar impact mechanism in their experiments, which modelled water flows impacting against a rigid barrier. They showed that the peak impact pressure on the barrier is inversely related to the radius of curvature formed at the base of the barrier as the water runs-up. By comparing the impact mechanisms of dry granular and water flow on a single rigid barrier, distinct differences in the impact mechanisms between dry granular and water flows highlight the importance of flow material on the impact dynamics. Ng et al. (2016) compared the impact dynamics of dry granular flow with viscous flow on a rigid barrier using centrifuge model tests. They reported that for the same initial conditions, the impact load resulting from dry granular flows was about 2.5 times smaller than that of viscous flows. They explained that the impact dynamics of dry granular and water flows are governed by frictional and viscous stresses, respectively. It was reported that energy dissipated by shearing of frictional contacts in dry granular flow is more significant compared to viscous shearing in water flows. Furthermore, the bulk

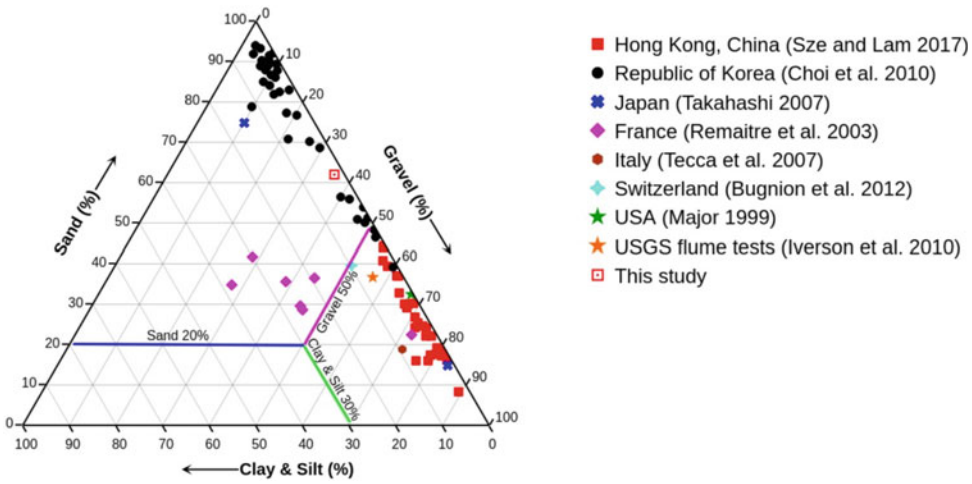

Fig. 13 Debris flow composition (particles of size larger than 20 mm were not sampled in Hong Kong cases)

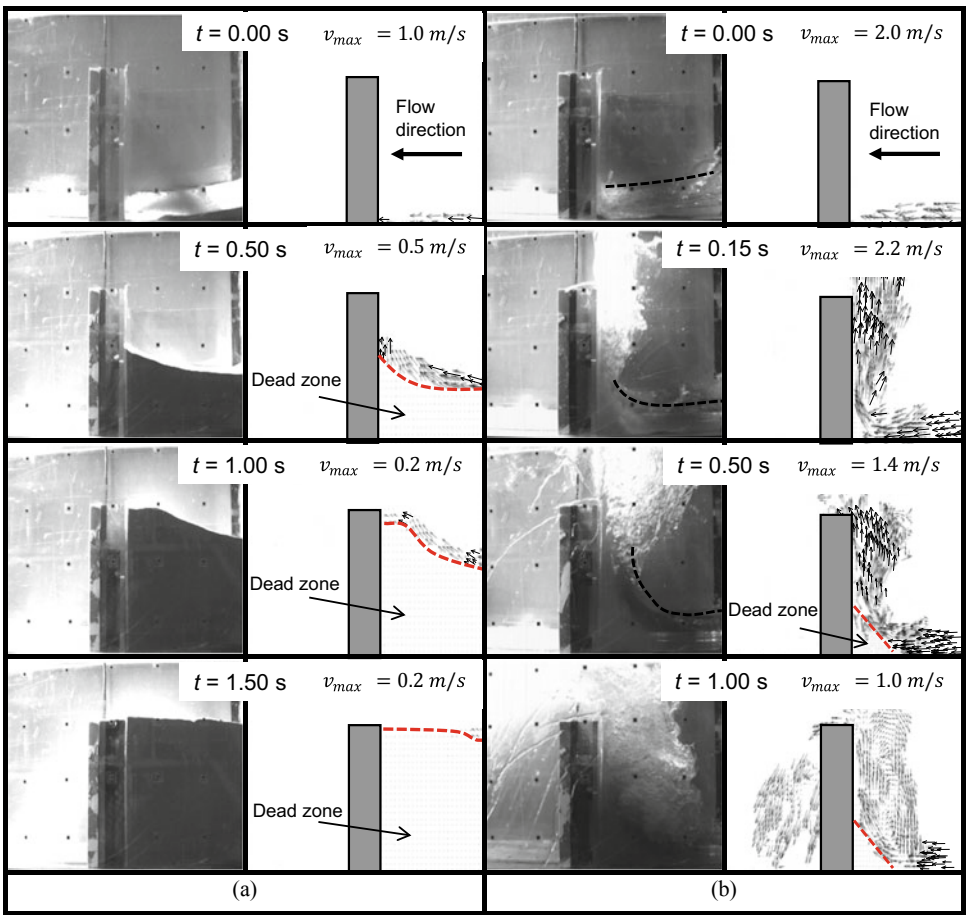

Fig. 14 Comparison of impact mechanisms in the 5 m-long flume for a single rigid barrier for: **a** dry granular flow; **b** water

compressibility of dry granular flow is much higher compared to water flows, resulting in more deformation and energy dissipation during impact. Therefore, granular flows induce lower impact forces. Song et al. (2017) reported a series of experiments modelling the impact dynamics of two-phase debris flows on a rigid barrier. As the volumetric solid content of the flow is increased, the impact mechanism transitioned from pileup to run-up. They also reported that the impact load increased with the volumetric solid content in the flow by up to 0.6, which is the typical volumetric solid content of typical debris flows observed in the field (Iverson 1997). Details of the measured impact forces in this study and their corresponding impact mechanisms are discussed later.

Single Flexible Barrier

Figure 15 shows a plan view of the impact kinematics of debris flow impacting against a single flexible barrier installed orthogonally to the channel bed. The test was carried out in the 28 m-long flume, which is inclined at an angle of 20°. Upon impact, the flow jumps along the face of the barrier at $t = 0.5$ s. Subsequent flow impacts the arrested material while some fines and fluid pass through the pervious flexible barrier. The dual spring elements were activated as the top cable deforms. The run-up follows the curvature of the deformed barrier and rolls back towards the upstream direction at $t = 1$ s. The original and deformed profiles of the top cable is shown using solid red and dashed white lines, respectively. As more debris deposits near the base of the barrier, the volume of material discharging through the barrier diminishes. The dual spring elements installed on the top and bottom cables were eventually fully mobilized. The bottom cables are no longer visible in the field of view due to the deformation of the flexible barrier along the flow direction. Overspill is observed at $t = 1.5$ s. Simultaneously, the rolling back motion of the debris flow front impacts the incoming flow and the dead zone increases in size. At $t = 2$ s the roll back diminishes and overspill continues. At $t = 5.0$ s, debris is retained by the flexible barrier with a horizontal free surface up to the fully deformed height of the barrier. The horizontal free surface of the deposit indicates a fluidized debris material.

The observed kinematics of debris flow impacting against the model flexible barrier exhibits characteristics of both run-up and pileup mechanism reported by Choi et al. (2015). Initially, the observed impact process in this study is reminiscent of the run-up mechanism. Near the end of impact, the observed impact mechanism resembles the pileup mechanism. More importantly, deformation and the perviousness of the barrier play important roles in the observed impact dynamics. The importance of barrier stiffness was demonstrated by Ng et al. (2020). They investigated the role of barrier stiffness on the peak impact force induced by dry granular flow impacting against a deformable barrier. They reported that barrier deformation during initial impact allows relative movement between the flow and a deformable

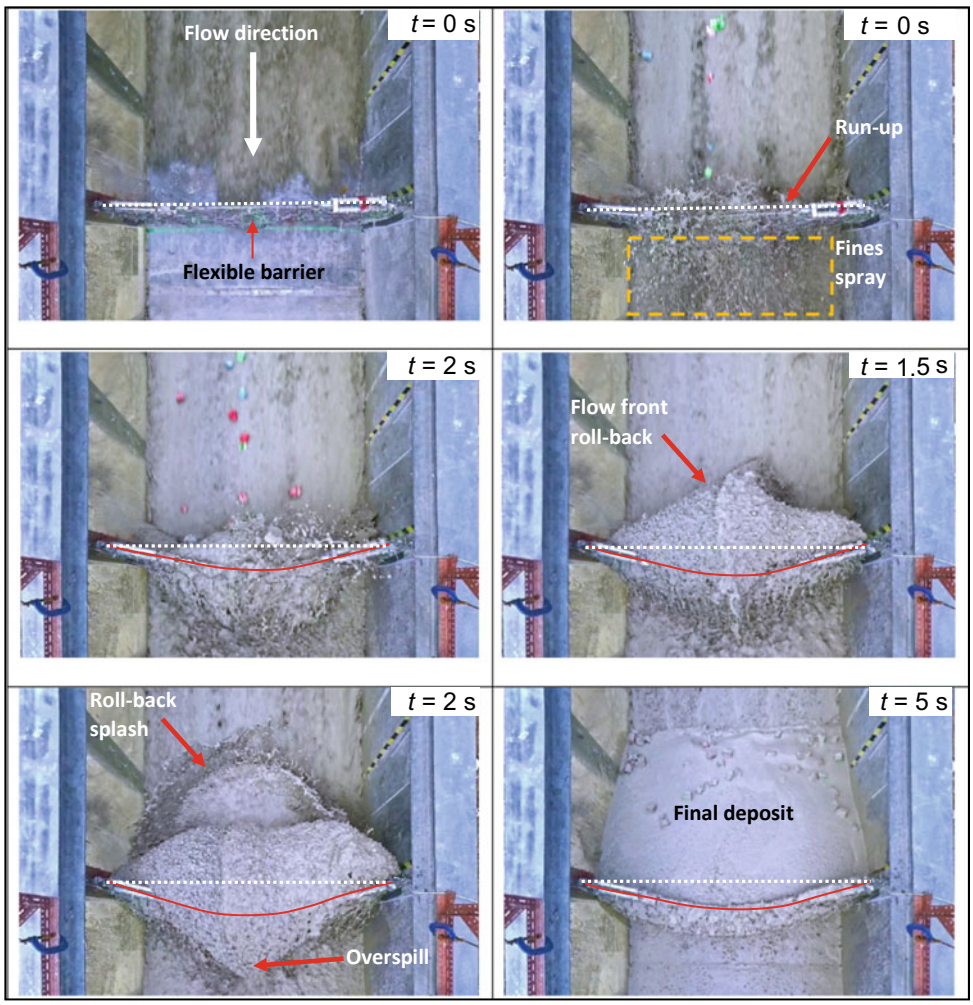

Fig. 15 Impact kinematics between two-phase debris flow and a flexible barrier in the 28 m-long flume

barrier, thereby extending the impact duration and attenuating the peak impact load. They showed that by reducing the bending stiffness of a typical 1-m thick concrete cantilevered barrier by five orders of magnitude (i.e. equivalent to a steel flexible barrier), the peak impact load was reduced by up to 40%. The importance of barrier perviousness was investigated by Liu (2019a). It was reported that compared to an impervious rigid barrier (Fig. 14), a pervious steel flexible barrier allows discharge through the barrier, thereby reducing the impact force induced on the barrier. The force induced on the flexible barrier is directly related to the rate of change in momentum. Thus, the effects of deformation and perviousness are both instrumental to the load attenuation mechanism of a flexible barrier (Volkwein 2014).

Rigid Barrier with Basal Clearance

Figure 16 shows the observed kinematics of dry granular flow, with 10 mm glass spheres, impacting against a model rigid barrier with a basal clearance. The kinematics, shown on the left, are captured using a high-speed camera, and the velocity fields, shown on the right, are analysed using PIV. The test was carried out using a 5 m-long flume inclined at 35°. The rigid barrier has a basal clearance with a ratio between basal clearance height and flow depth H_c/h_0 of 0.7. The thin tapered flow front initially passes through the basal clearance since the flow depth is less than the height of the basal clearance. Discharge underneath the barrier reduces the momentum transferred to the barrier, thereby reducing the impact force on the barrier. As the saltating front increases in depth (Fig. 16a), part of the flow impacts the base of the barrier. After impact, some particles are observed to rebound off the barrier and collide with incoming particles. The collisions lead to the rapid deceleration and redirection of subsequent flow upwards along the face of the barrier. This change in impact direction is shown by the PIV vectors. The measured maximum flow velocity from PIV analysis at this moment (t = 0.15 s; Fig. 16a) was 2.8 m/s, which reduced by 10% compared with initial impact velocity. As more granular flow impacts the barrier, granular material accumulates behind the rigid barrier above the basal clearance as shown by the dead zone observed in the PIV analysis (Fig. 16b). Concurrently, the vertical stress near the basal clearance increases with retained height of material and a reduction in discharge velocity underneath the barrier by up to 75% is observed (Fig. 16c).

Dual Rigid Barriers

Figure 17a shows the kinematics of dry granular flow impacting dual rigid barriers installed orthogonally to the channel bed. The flume is inclined at an angle of 35° to the horizontal. The flow front reaches the first barrier at t = 0 s and runs-up. Incoming flow material piles up in layers behind the barrier up to the height of the barrier. At t = 0.5 s the first barrier is filled, and cascading overflow is observed. The first barrier gets filled to the crest in a similar manner as that shown in Fig. 14 for a single rigid barrier and similar to the proposed velocity attenuation model (Fig. 6). At t = 1 s, the overflow lands on the flume base and flows downstream to impact the second barrier. The overflow impacts the flume base following a trajectory described by Eq. 4 at an angle of 30° measured relative to the flume base. The measured landing angle $\beta = 30^{\circ}$ corresponds to a landing factor $C_r = 0.87$ (Eq. 5 with R = 1). The energy dissipated during landing attenuates the flow velocity between the first and second barriers, thus reducing the impact load induced on the second barrier. As the impact process on the second barrier continues, the wedge of deposited dry granular material accumulates behind the second barrier and propagates upstream. The upstream movement of granular material eventually intercepts the overflow from the first barrier at t = 1.5 s. From t = 1.5 s to t = 3 s, overflow continues to impact the downstream deposition wedge, thereby enlarging the deposition volume. The end of impact process is marked at t = 25 s, when the dry granular material has come to rest.

Figure 17b shows the kinematics of water flow impacting against dual rigid barriers installed orthogonally to the channel bed. The flume is inclined at an angle of 10° to the horizontal. The flow front reaches the first barrier at t = 0 s and runs-up along the barrier face at t = 0.5 s. The initial impact kinematics are similar to those described in Fig. 14b for a single rigid barrier resisting water flow. However, the impact process in Fig. 17b is different compared to Fig. 14b for a single barrier once the barrier is filled to the crest and water overflows the first barrier. The difference between the impact kinematics of dry granular flow and water flow also emerges between t = 0.5 s–t = 1.0 s. Compared to dry granular overflow, water overflow lands on the flume at a steeper angle. As a result, water overflow lands closer to the first barrier compared to dry granular flow. Significant turbulence is observed for water overflow, thus the landing angle at t = 1 s cannot be deduced. At t = 1.5 s, the impact process at the first barrier ends as water upstream of the barrier comes to rest. The water that landed in between the two barriers flows downstream and impacts the second barrier. The impact process ends at t = 6 s with water flow arrested by the dual barriers.

Overflow kinematics and impact dynamics of dual rigid barriers for both dry granular and water flows observed in the above experiments are used to verify the proposed analytical framework and discussed in detail later.

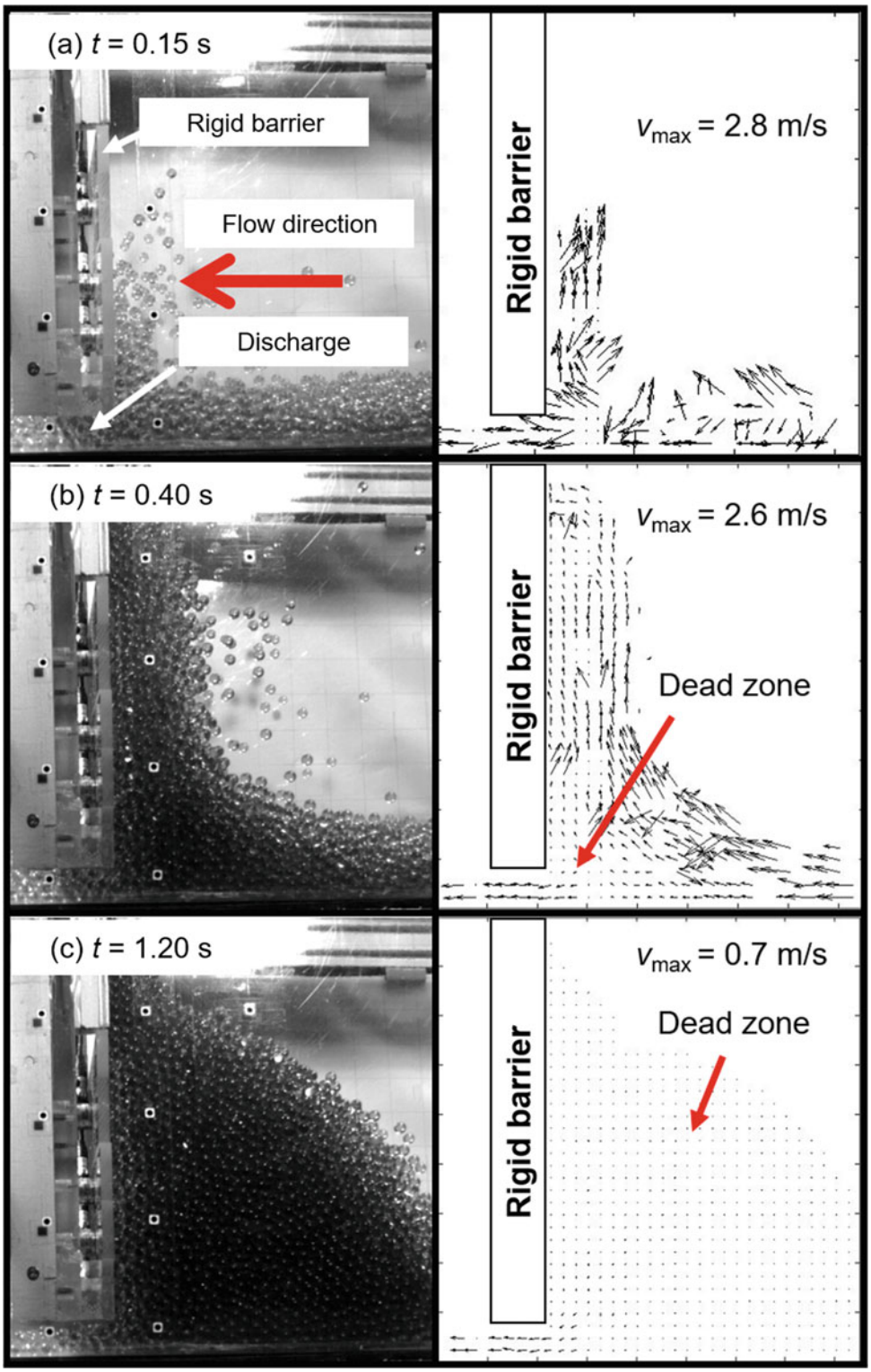

Fig. 16 Flume modelling of the rigid barrier with basal clearance of relative opening $H_c/h_0 = 0.7$ (with 35^0 flume inclination): Observed dry granular flow kinematics (left) and PIV analysis (right)at **a** $t = 0.15$ s; **b** $t = 0.40$ s; **c** $t = 1.20$ s (Choi et al. 2020)

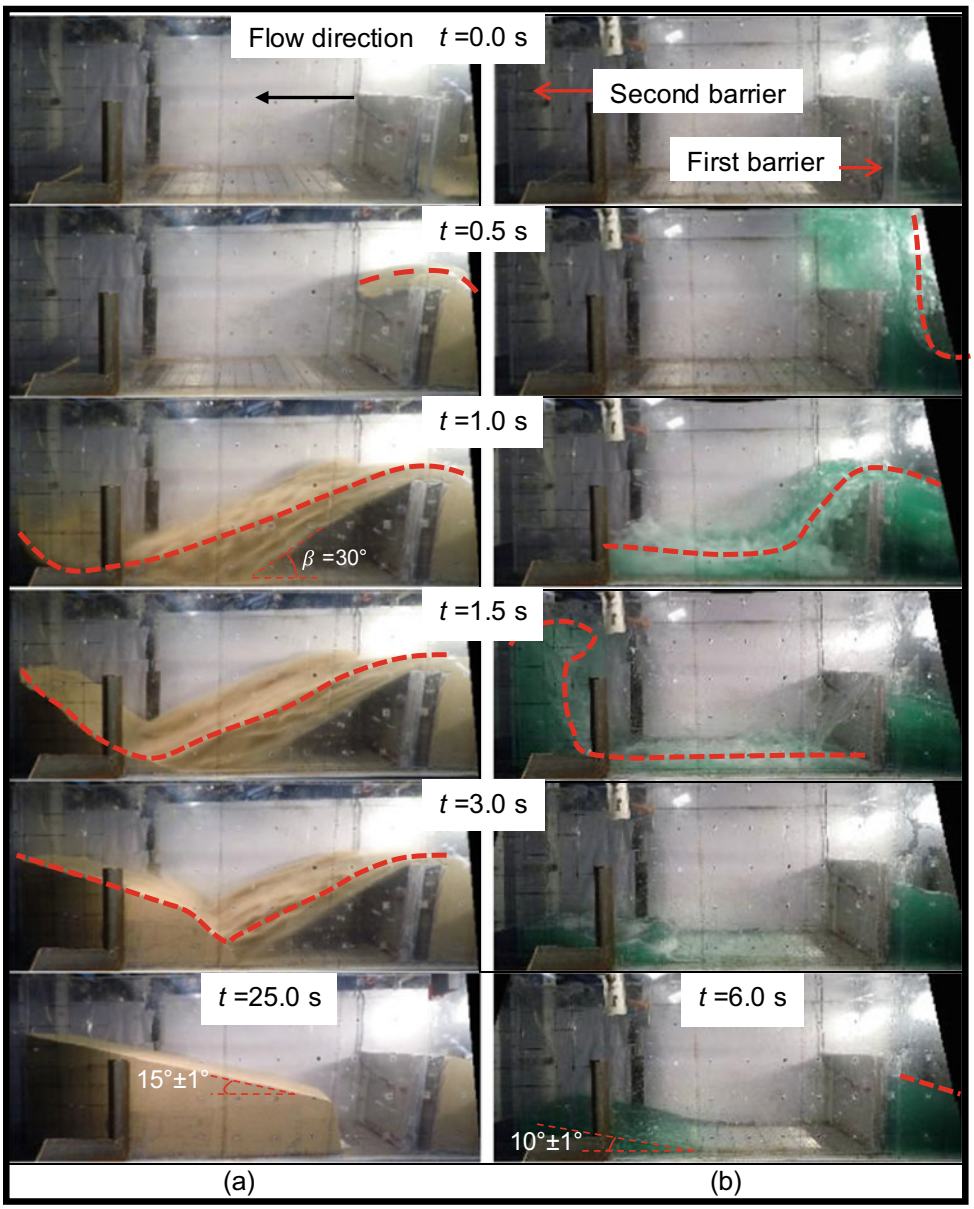

Fig. 17 Comparison of overflow and landing mechanisms in 5 m-long flume for dual-rigid barriers: **a** dry granular flow; **b** water

Estimating the Impact Load on Single Barriers with and Without Basal Clearance

The peak load induced on a barrier is the sum of the dynamic and static components of the flow. The relative contributions of the dynamic and static loads to the peak load is related to the Froude number (Fr) of the flow before impact (Faug 2015). Furthermore, the Froude number in turn is strongly influenced by the geomorphological settings. For example, in Hong Kong, debris flows travel at high velocities on steep terrain over short distances. These conditions may lead to higher Froude numbers ($Fr > 3$). In contrast, the Froude conditions in the Alps or Rockies tend to be lower ($Fr < 3$) because flows travel on gentler terrain.

Figure 18 shows the relationship between the Froude number and the peak load F_{peak} normalised by the theoretical static load $F_{static} = 0.5k\rho gh_0^2 w$(Armanini and Scotton 1993; Armanini 2009) of the flow before impact, which can be calculated as follows:

$$\frac{F_{peak}}{0.5k\rho gh_0^2 w} = 1 + \frac{2\alpha}{k}Fr^2 \tag{6}$$

Existing design guidelines in Hong Kong adopt a static impact coefficient $k = 1$ (no internal shear strength) and $\alpha = 2.5$ for rigid barriers (Kwan 2012), and $k = 1$ and $\alpha = 2$ for flexible barriers (Kwan and Cheung 2012). It is worthwhile to note that the α recommended by Kwan (2012) and Kwan and Cheung (2012) accounts for hard and large

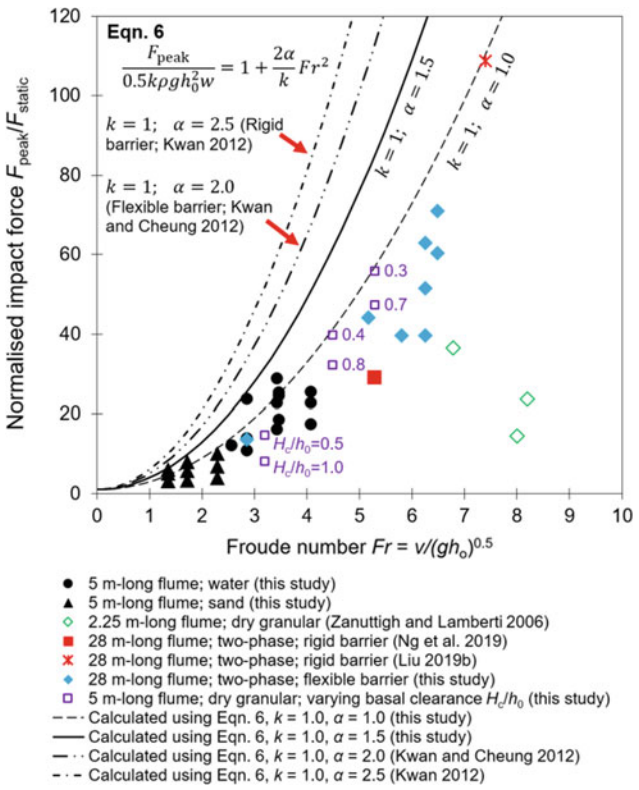

Fig. 18 Design Froude number for single rigid and flexible barrier against debris flow impact

inclusions. These design parameters are used in Eq. 6 and compared to the measured data. In addition, two theoretical bounding lines using Eq. 6 are shown. The first theoretical bounding line adopts $k = 1$ and $\alpha = 1$. The second theoretical bounding line using $k = 1$ and $\alpha = 1.5$. Details of the bounding lines are discussed below.

Compared to the existing design guidelines in Hong Kong for rigid barrier ($k = 1$ and $\alpha = 2.5$), the theoretical bounding line ($k = 1$ and $\alpha = 1.5$) conservatively estimates all the measured data in this study for dry granular, water, and two-phase debris flows, and for dry granular flow from Zanuttigh and Lamberti (2006). The data falls within a range of Froude numbers from 0 to 9. Thus, the theoretical bounding line ($k = 1$ and $\alpha = 1.5$) can provide load optimisation for rigid barrier design. A summary of the recommended design parameters is given in Table 3.

Compared to the existing design guidelines in Hong Kong for flexible barrier ($k = 1$ and $\alpha = 2$), the theoretical bounding line ($k = 1$ and $\alpha = 1$) conservatively estimates the impact force for all flexible barrier data points for two-phase debris flows and provide opportunities for load optimisation for flexible barrier design.

The dry granular flows in this study exhibited lower normalised impact forces compared to the water flows in the 5-m flume tests. This may be attributed to a higher degree of bulk compressibility and internal energy dissipation mainly due to friction in dry granular flows leading to higher energy dissipation during the impact process (Choi et al. 2015). Both of these features, compressibility and enduring frictional contacts, led to a pileup mechanism. Similarly, the dry granular flows reported in the literature (Zanuttigh and Lamberti 2006) for higher Froude numbers ($Fr > 4$) also tend to exhibit lower impact force compared to two-phase debris flows (Ng et al. 2019) in which the flows were almost incompressible.

A comparison of the normalised peak impact loads resulting from dry granular flow impacting rigid barriers with different basal clearances is shown. The basal clearance H_c is normalised by the maximum flow depth h_o. In the experiments, glass spheres with a uniform particle size of 10 mm were used. The impact load decreases with an enlarging basal clearance height under a same Froude condition. The theoretical bounding line ($k = 1$ and $\alpha = 1$) provides a conservative estimate of the impact load for basal clearances $H_c/h_o \leq 1.0$ and can be adopted for designing rigid barriers with a basal clearance (see Table 3).

Evaluation of Analytical Framework for Dual Rigid Barriers

Verification of the analytical framework for dual rigid barriers (Eqs. 2, 4, and 5) from physical experimental results from the 5 m-long and 28 m-long flumes is discussed below.

Run-up velocity (v_d)

Figure 19 shows a comparison of the measured and calculated normalised run-up heights (h_d/h_0) and normalised

Table 3 Design recommendations for estimating the impact loads for different barrier configurations

Design recommendations#	Dynamic impact coefficient (α)
Single rigid barrier without basal clearance	1.5
Single rigid barrier with basal clearance ($0.3 \leq H_c/h_0 \leq 1.0$)	1.0
Single flexible barrier	1.0
The second barrier in a dual rigid barrier system	1.0

A static impact coefficient $k = 1.0$ is recommended to deduce static load

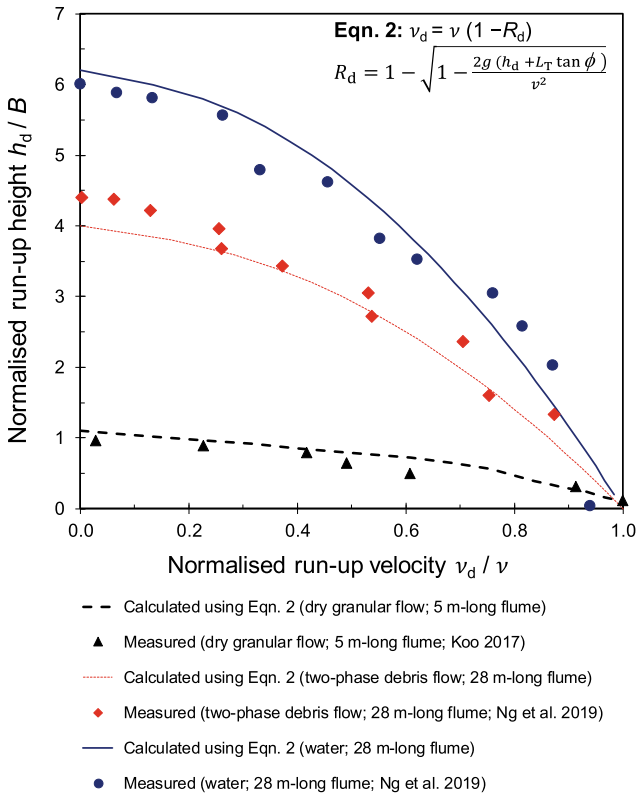

Fig. 19 Comparison of measured and calculated run-up velocity with barrier height (modified from Ng et al. 2018)

run-up velocities (v_d/v) for dry granular (Koo 2017), water (Ng et al. 2019) and two-phase debris flows (Ng et al. 2019) impacting a rigid barrier. Dry granular flow impacting a rigid barrier was modelled using the 5 m-long flume. The run-up velocity v_d is normalised by the flow velocity v before impacting the rigid barrier, whereas the run-up height h_d is normalised by the maximum flow depth h_0. Water and two-phase debris flows impacting a rigid barrier were modelled using the 28 m-long flume. The calculated run-up velocity was determined using the velocity attenuation model (Fig. 6). The initial flow velocity measured in the physical experiments is used to calculate the attenuation of velocity during impact by using Eq. 2. Therefore, the measured and calculated velocities at the base of the barrier are the same. The calculated velocities for the dry granular tests agree with the measured velocities. Similarly, the results of the two-phase debris flows from the 28 m-long flume tests for rigid barrier show reasonable agreement with the calculated values. Dry granular flows exhibit lower run-up heights compared to water flows. The run-up of two-phase debris flow lies closer to the water flows even with 60% solid fraction. This run-up height may be attributed to fluidization of the two-phase material due to sustained excess pore fluid pressure during impact (Ng et al. 2019). A summary of the parameters used to deduce the run-up velocity is given in Table 4.

Overflow Distance (x_i)

The launch angle of the overflow from the first barrier determines the trajectory and overflow distance. Figure 20 compares the measured and calculated overflow distances for dry granular flow, water and two-phase debris flows. The calculated values are obtained by using Eq. 4. The effects of barrier height and flume inclination on overflow distance are examined. The overflow distance x_i and barrier height B are normalised by the flow depth h_o before the flow impacts the rigid barrier. In the tests conducted with dry granular, the normalised barrier height B/h_0 varies as 1.1, 2.0 and 2.9 for a flume inclination of 26° and as 1.0, 1.9 and 2.7 for a flume inclination of 32°. These heights correspond to typical barrier designs observed in the field. The inclination of the flume was adjusted to vary the flow inertia before impact. In contrast with the tests for dry granular flow, the flume inclination was fixed to be 20° for the two-phase debris flow and water flow tests conducted in the 28 m-long flume. Normalised barrier heights B/h_0 of 5.5 and 5.0 are used for the two-phase debris and water flows, respectively. A comparison of the measured results of dry granular impacting different barrier heights shows that the overflow distance decreases with increasing barrier height. More energy is dissipated from shearing among grains and the conversion of kinetic energy to potential energy as the barrier height increases. High flume inclinations lead to more inertial flows before impact, thereby causing longer overflow distances. A comparison between measured and calculated overflow distances for dry granular flow shows that calculated distances using Eq. 4 can provide reasonable estimates and are on the conservative side.

The measured overflow distances downstream from the first barrier were 4.5 m and 3.3 m for the water and two-phase debris flows, respectively. The measured overflow distance for both flows is somewhat lower than that calculated, but on the conservative side. Evidently, Eq. 4 can provide a reasonable estimate of the overflow distance for all three types of flows investigated in this study. The minimum barrier spacing required between the successive barriers should ensure that the flow lands between two barriers.

Landing Factor (C_r)

The landing factor C_r (Eq. 5) accounts for the momentum loss from the impact between the flow and the flume bed. Physically, momentum is assumed to be completely

Table 4 Parameters for calculating run-up velocity (v_d)

Parameter	Value	Flow type	Method of determination	
			This study	Remark
Initial impact velocity, v (m/s)	2.0	Water	Measured	Velocity hydrograph from debris mobility analysis
	6.0	Debris flow		
	1.0	Dry granular		
Initial flow depth, h_0 (m)	0.060	Water	Measured	Flow depth hydrograph from debris mobility analysis
	0.065	Debris flow		
	0.090	Dry granular		
Friction angle, (º)	–	Water	–	–
	0	Debris flow	Deduced from deposition angle	Measured deposition angle is zero
	30	Dry granular	Measured	Material dependent
Angle of deposition θ_d (º)	0	Water	Measured	Assume same as
	0	Debris flow		
	30	Dry granular		
Height of the deposited granular material, h_d (m)	Varies	Water	Measured in stages	Initially assume $h_d = h_0$; Calculate h_d for successive stages by adding h_o/sin $(\theta_d - \theta)$; θ is the channel slope Number of stages = B/h_0; Fig. 6
		Debris flow		
		Dry granular		
Length of the free surface of the arrested granular material, L_T (m)	Varies	Water	Measured in stages	Using Fig. 6 geometry calculate as $L_T = h_d / \sin(\theta_d - \theta)$
		Debris flow		
		Dry granular		

Acceleration due to gravity (g = 9.81 m/s^2)

destroyed when flow lands perpendicularly to the flume with $\beta = 90°$ or $C_r = 0$. In contrast to the perpendicular impact, no energy is dissipated when flow lands tangentially to the flume bed with $\beta = 0°$ or $C_r = 1$. Figure 21 compares the estimated landing factors C_r using Eq. 5 and those back-calculated from the flume experiments of dry granular flows in a 5 m-long flume (Koo 2017) and two-phase debris flows in a 28 m-long flume (Ng et al. 2019). The back-calculated C_r is for dry granular flows landing on the acrylic bed of the 5 m-long flume and a two-phase debris flow landing on the steel bed of the 28 m-long flume. The landing angle from the water flow is not included in the figure because the water flow was turbulent when it landed, thereby making it impossible to determine the landing velocity.

It is evident that the landing factor C_r increases for dry granular flow as the landing angle decreases, thereby implying that less energy is dissipated upon landing. A best fit line through the measured data is shown to reveal the contribution of the energy dissipated via basal friction upon landing. The projected best fit gives an R coefficient of 0.9 at $= 0°$. This result indicates that energy dissipation from the tangential shear between the flow and the bed is only 10% of the total energy dissipated upon landing. Nonetheless, a value of $R = 1$ (no energy loss from the tangential bed shear) provides an upper bound for the dry granular and two-phase debris flows. The results imply that Eq. 5 with $R = 1$ can be used to estimate the landing factor C_r.

The impact dynamics in a dual rigid barrier system can be calculated at different stages of impact process. The frontal

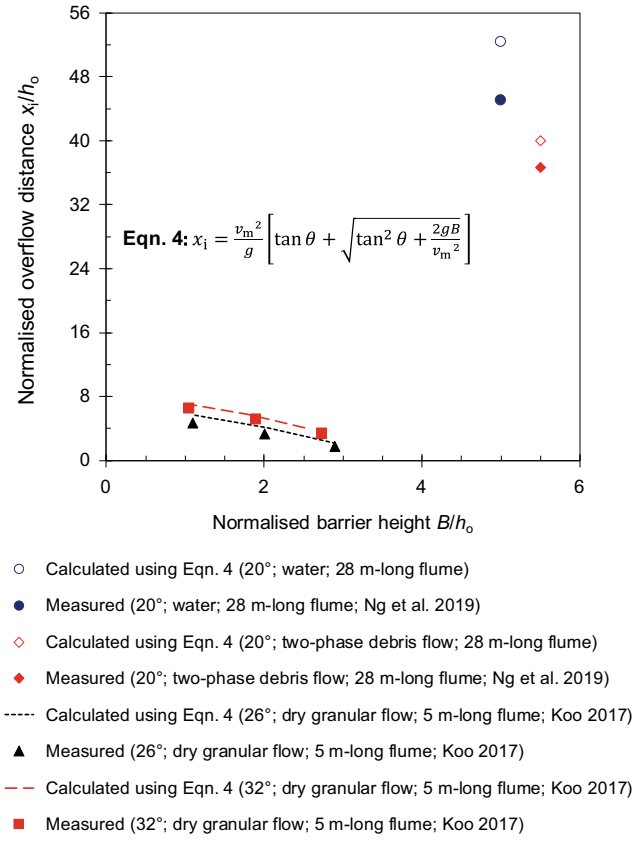

Fig. 20 Effects of flume inclination and barrier height on overflow distance (modified from Ng et al. 2018)

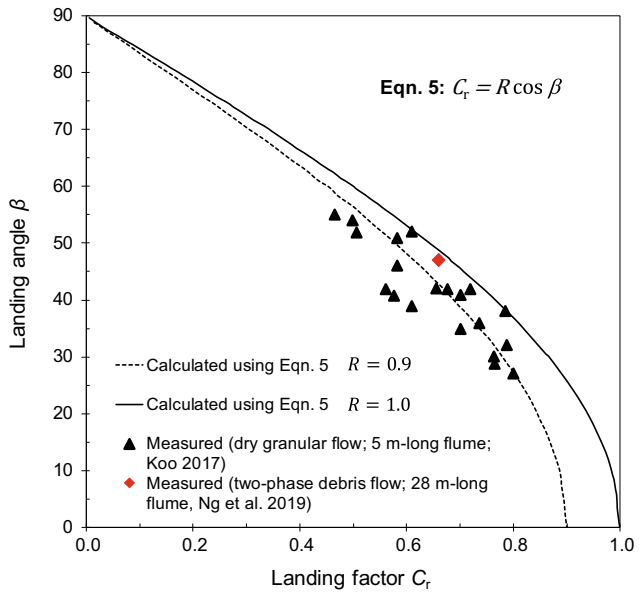

Fig. 21 Comparison of landing factor (modified from Ng et al. 2018)

velocity is an indicator of flow attenuation and acceleration at different stages of the impact process. Three different frontal velocities for the two-phase debris flow test are compared in Fig. 22 to evaluate the entire multiple barrier analytical framework in Eqs. (2)–(5). The calculated and measured velocities before impact, during overflow and after landing are compared.

The frontal velocity of the two-phase debris flow before impacting the first barrier was 6 m/s. This pre-impact velocity was adopted as the initial input for Eqs. (2)–(4). The resulting calculated overflow velocity at the crest of the barrier is 5.7 m/s, which is close to the measured velocity, which was 5.4 m/s. Furthermore, the measured velocity after landing was 3 m/s, and the measured landing angle was 48° ± 2° (C_r = 0.66). Notably, water overflow landing in the channel was turbulent, thereby making it impossible to measure the landing velocity correctly. Hence, the test result for water flow is not included.

Velocity reduction upon landing depends on the landing angle, the flow composition and the flume bed. Kwan et al. (2015) reviewed data from the field and laboratory tests. The data includes dry granular and two-phase debris flows impacting hard and/or soft beds. The reported velocity reduction factors C_r range from 0.3 to 0.75. The calculated post-landing velocity, by using a C_r of 0.7 and the measured velocity are compared. The calculated landing velocity is

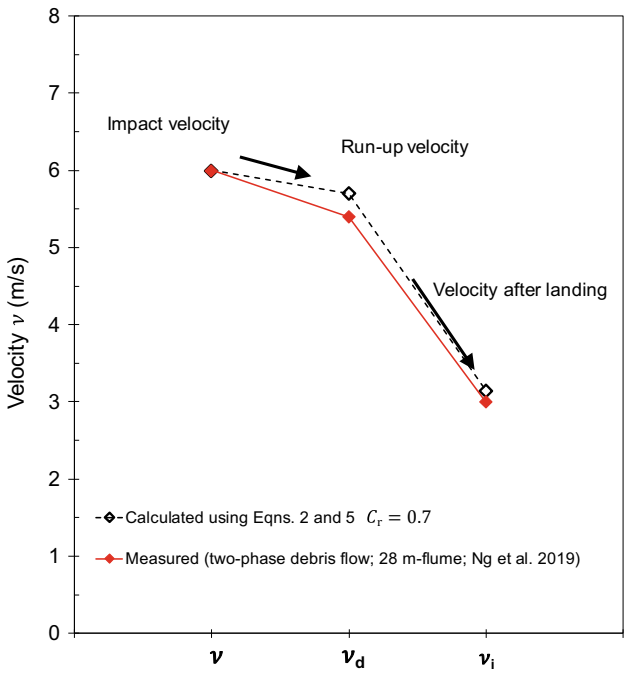

Fig. 22 Comparison of measured and calculated frontal velocity for dual rigid barrier system (modified from Ng et al. 2019)

3.2 m/s, which agrees well with the measured post-landing velocity (3 m/s) for a two-phase debris flow impacting a steel flume bed in the 28 m-long flume. Therefore, $C_r = 0.7$ is recommended to estimate the post-landing velocity.

Impact Force on Second Rigid Barrier

Design guidelines for multiple rigid barriers in series are not yet available. Current approaches for designing multiple barriers adopt a similar principle as that for a single barrier (Kwan 2012). The single barrier approach does not consider the effects of the upstream barriers on attenuating the impact forces on the downstream barriers. Figure 23 shows the relationship between the normalized peak impact force and flow Froude number for the second rigid barrier of a dual barrier system that is investigated in this study. Similarly to Fig. 18, the measured peak impact forces (F_{peak}) for dry granular flows and water are normalized by the theoretical static force (F_{static}) $0.5k\rho g h_0^2 w$. To obtain conservative impact forces on the second barrier, the flow depth before impacting the second barrier is assumed to remain constant and equal to the flow depth at the first barrier. Both water and dry granular flow data from the 5 m-long flume experiments are compared. Generally, the Froude numbers of the dry granular flows have lower Froude numbers compared to those of the water flows because more energy dissipation occurs via frictional shearing among grains (Choi et al. 2015). The normalized impact forces exerted by water flows are higher than those exerted by dry granular flows because water overflow lands closer to the first barrier compared to dry granular overflow, resulting in sufficient length for flow acceleration (Fig. 17). The measured impact forces are compared with the theoretical normalized peak impact force (Eq. 6). In comparison with the upper bound for a single rigid barrier (Fig. 18) where $k = 1$ and $\alpha = 1.5$, an upper bound with $k = 1$ and $\alpha = 1$ (refer to Table 3) provides a conservative estimate of the impact force exerted on the second barrier as shown in Fig. 23. The reduction of normalized peak impact forces for the second barrier is mainly attributed to the energy dissipation during impact on the first barrier and landing between the dual barriers.

In summary, the newly proposed analytical framework for designing a multiple rigid barrier system by considering the velocity attenuation during impact, overflow and landing has been verified by the experimental data shown in this study. The attenuated flow velocity at the crest of the first barrier (Fig. 19) is used to estimate the overflow velocity and distance (Fig. 20). Landing reduction factors (Fig. 21) are then implemented to obtain the flow velocity after landing (Fig. 22). This velocity is then adopted to estimate the impact force on the second barrier (Fig. 23). The analysis can be carried out repeatedly to predict the impact loads on the third and any subsequent barriers installed downstream in the channel.

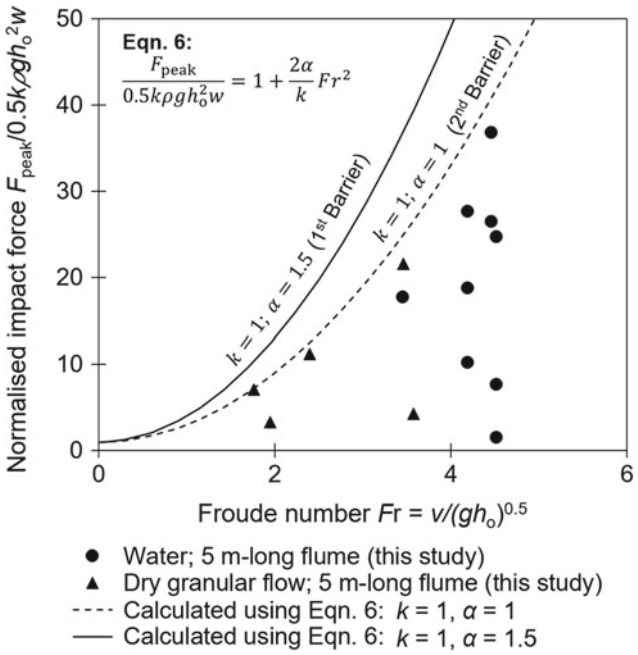

Fig. 23 Design impact force for first and second rigid barrier in dual barrier system

Summary and Conclusions

This forum paper presents a collection of physical experiments modelling the impact mechanisms against single and dual rigid barriers and a single flexible barrier. The flow types examined include dry granular, water and two-phase flows. Additionally, the effects of a basal clearance on the impact dynamics of dry granular flow on a single rigid barrier were examined. Experiments were conducted at two different scales, including 5 m-long and 28 m-long flumes. Based on the observed fundamental impact mechanisms, impact load measurements were compared with a newly developed analytical framework for designing multiple rigid barriers.

The design load for a single rigid barrier without a basal clearance should be estimated using an $\alpha = 1.5$. The static load should be estimated using $k = 1$. The design load for a single rigid barrier with a basal clearance ($0.3 \leq H_c/h_0 \leq 1.0$), a single flexible barrier, and the second rigid barrier in a dual rigid barrier system should be estimated using an $\alpha = 1.0$. It should be noted that large and hard inclusions were not explicitly considered in this study. Therefore, some α values proposed in other design guidelines are higher than those recommended in this study.

The newly proposed multiple barrier framework was verified using experimental data. The attenuated velocity v_d along the barrier height can be predicted reasonably well using the velocity attenuation model. The horizontal overflow distance x_i can be conservatively estimated by the proposed equation. The minimum barrier spacing should be kept larger than the calculated overflow distance to ensure a robust multiple barrier design. Based on the experimental data, a landing factor of $C_r = 0.7$ gives a conservative estimate of flow velocity before the second barrier. This estimated velocity serves as the initial input velocity for the design of the next barrier along the flow path.

Looking Ahead

Given that debris flow is scale-dependent, the development and construction of the largest testing facilities possible will be necessary to advance the current state of scientific and engineering understanding on utilising barriers to mitigate debris flows. The world's largest man-made flume is currently under construction. This facility is jointly developed between The Hong Kong University of Science and Technology and the Institute of Mountain Hazards and Environment of the Chinese Academy of Sciences. The model is 172 m in length, 6 m in width and has an inclination of up to 30º (Fig. 24). The storage container at the most upstream end of the slope can store a debris volume of 500 m^3. This facility will not only be used to evaluate the proposed multiple barrier framework in this study, but serve the local and international scientific and engineering community at large for decades to come.

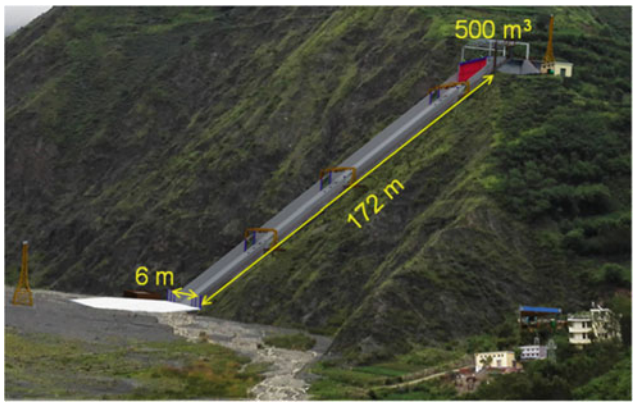

Fig. 24 Schematic of 172 m-long flume (Kunming, China)

Acknowledgements The authors are grateful for financial support from the theme-based research grant T22-603/15-N and area of excellence project grant AoE/E-603/18, as well as the general research fund grants 16212618, 16209717, and 16210219 provided by the Research Grants Council of the Government of Hong Kong Special Administrative Region, China. The authors are immensely grateful for the support from the National Natural Science Foundation of China (51,709,052). This paper is published with the permission of the Head of the Geotechnical Engineering Office and the Director of Civil Engineering and Development, Hong Kong SAR Government.

References

Armanini A (2009) Discussion on: Experimental analysis of the impact of dry avalanches on structures and implication for debris flow (Zanuttigh, Lamberti). J Hydraul Res 47(3):381–383

Armanini A, Scotton P (1993) On the dynamic impact of a debris flow on structures. In Proceedings of XXV IAHR Congress, Tokyo (Tech. Sess. B, III), 203–210

Armanini A, Rossi G, Larcher M (2019) Dynamic impact of a water and sediments surge against a rigid wall. J Hydraul Res 58(2):314–325

ASI (2008) ONR 24801. Austrian Standard Institute, Austria, Protection Works for Torrent Control - Actions on Structures (Draft), p 25

Berger C, McArdell BW, Schlunegger F (2011) Direct measurement of channel erosion by debris flows, Illgraben, Switzerland. J Geophys Res Earth Surf 116:F01002

Bonnet-Staub I (1999) Definition d'une typologie des deposits de laves torrentielles et identification de critres granulomtriques et geotechniques concernant les zones sources. J Bull Eng Geol Environ 57 (4):359–367

Brighenti R, Segalini A, Ferrero AM (2013) Debris flow hazard mitigation: a simplified analytical model for the design of flexible barriers. Comput Geotech 54:1–15

Bugnion L, McArdell BW, Bartelt P, Wendeler C (2012) Measurements of hillslope debris flow impact pressure on obstacles. Landslides 9(2):179–187

Development Bureau (2020) Geotechnical engineering office built a debris-resisting barrier in Tung Chung to reduce the risk of landslides on natural hillsides [online]. Available from https://www.devb.gov.hk/filemanager/tc/content_1044/20180204_08.html [cited 13 April. 2020]

Choi YJ (2010) A study on downstream process of debris flow mobilized from landslides, Master Thesis, Kangwon National University, Korea

Choi CE, Au-Yeung SCH, Ng CWW, Song D (2015) Flume investigation of landslide granular debris and water runup mechanisms. Géotech Lett 5(1):28–32

Choi CE, Ng CWW, Liu H, Wang Y (2020) Interaction between dry granular flow and rigid barrier with basal clearance: analytical and physical modelling. Can Geotech J 57(2):236–245

DeNatale JS, Iverson RM, Major JJ (1999) Experimental testing of flexible barriers for containment of debris flows. US Department of the Interior, US Geological Survey

Faug T, Caccamo P, Chanut B (2012) A scaling law for impact force of a granular avalanche flowing past a wall. Geophys Res Lett 39(23): L23401

Faug T (2015) Macroscopic force experienced by extended objects in granular flows over a very broad Froude-number range: macroscopic granular force on extended object. Eur Phys J E 38:13–16

Froude MJ, Petley DN (2018) Global fatal landslide occurrence from 2004 to 2016. Nat Hazards Earth Syst Sci 18:2161–2181

Iverson RM (1997) The physics of debris flows. Rev Geophys 35 (3):245–296

Iverson RM (2015) Scaling and design of landslide and debris-flow experiments. Geomorphology 244:9–20

Iverson RM, George DL (2014) A depth-averaged debris-flow model that includes the effects of evolving dilatancy. I. Physical basis. Proceedings of the royal society a: mathematical, Physical and Engineering Sciences 470(2170):20130819

Iverson RM, Logan M, LaHusen RG, Berti M (2010) The perfect debris flow? aggregated results from 28 large-scale experiments. J. Geophys. Res. Earth Surf. 115:F03005

Jakob M, Stein D, Ulmi M (2012) Vulnerability of buildings to debris flow impact. Nat Hazards 60:241–261

Koo RCH (2017) Mechanisms of interaction between dry sand flow and multiple rigid barriers: flume and finite-element modelling. Ph. D Thesis, The Hong Kong University of Science and Technology, Hong Kong, China

Koo RCH, Kwan JSH, Ng CWW, Lam C, Choi CE, Song D, Pun WK (2017) Velocity attenuation of debris flows and a new momentum-based load model for rigid barriers. Landslides 14(2):617–629

Kwan JSH (2012) Supplementary technical guidance on design of rigid debris-resisting barriers, Technical Note No. TN 2/2012. Hong Kong, SAR China, Geotechnical Engineering Office, Civil Engineering and Development Department, The HKSAR Government

Kwan JSH, Cheung RWM (2012) Suggestion on design approaches for flexible debris resisting barriers. Discussion note DN1/2012. Hong Kong, SAR China, Geotechnical Engineering Office, Civil Engineering and Development Department, The HKSAR Government

Kwan JSH, Koo RCH (2015) Enhanced Technical Guidelines for Design of Debris-resisting Barriers. GEO Report No. 333. Hong Kong, SAR China, Geotechnical Engineering Office, Civil Engineering and Development Department, The HKSAR Government

Kwan JSH, Koo RCH, Ng CWW (2015) Landslide mobility analysis for design of multiple debris-resisting barriers. Can Geotech J 52 (9):1345–1359

Liu HD (2019a) Effects on mesh size on the impact mechanism of debris flow impacting net barriers. Ph.D Thesis, The Hong Kong University of Science and Technology, Hong Kong, China

Liu HM (2019b) Impact mechanisms of debris flow against multiple rigid barriers with basal clearance. PhD Thesis, The Hong Kong University of Science and Technology, Hong Kong, China

Lo DOK (2000) Review of natural terrain landslide debris-resisting barrier design. Geotechnical Engineering Office, Hong Kong, SAR, China, p 91 (GEO report no. 104)

Ng CWW, Song D, Choi CE, Koo RCH, Kwan JSH (2016) A novel flexible barrier for landslide impact in centrifuge. Géotech Lett 6 (3):221–225

Ng CWW, Choi CE, Koo RCH, Goodwin GR, Song D, Kwan JSH (2018) Dry granular flow interaction with dual-barrier systems. Géotechnique 68(5):386–399

Ng CWW, Choi CE, Majeed U, Poudyal S, De Silva WARK (2019) Fundamental framework to design multiple rigid barriers for resisting debris flows. In: Proceedings of the 16th asian regional conference on soil mechanics and geotechnical engineering. 14th to 18th October 2019. Taipei, Taiwan, China

Ng CWW, Wang C, Choi CE, De Silva WARK, Poudyal S (2020) Effects of barrier deformability on load reduction and energy dissipation of granular flow impact. Comput Geotech 121:103445

NILIM (2007) Manual of technical standard for establishing Sabo master plan for debris flow and driftwood. Technical Note of NILIM No. 364. Natural Institute for Land and Infrastructure Management, Ministry of Land, Infrastructure and Transport, Japan. [In Japanese.]

Piton G, Recking A (2015) Design of sediment traps with open check dams. I: hydraulic and deposition processes. J Hydraul Eng 142 (2):04015045

Remaitre A, Malet JP, Maquaire O, Ancey C (2003) Study of a debris-flow event by coupling a geomorphological and a rheological investigation, example of the Faucon stream (Alpes-de-Haute-Provence, France), Debris-Flow Hazards Mitigation, Mechanics, Prediction, and Assessment, eds. Rickenmann and Chen. Millpress, Rotterdam, pp 375–385

Rickenmann D (1999) Empirical relationships for debris flows. Nat Hazards 19:47–77

Song D, Ng CWW, Choi CE, Zhou GGD, Kwan JSH, Koo RCH (2017) Influence of debris flow solid fraction on rigid barrier impact. Can Geotech J 54(10):1421–1434

Sze EHY, Lam HWK (2017) Some suggested detailing of flexible net barriers traversing a stream course for drainage purposes, GEO Technical Note TN 3/2017. Geotechnical Engineering Office, Hong Kong, SAR, China

Takahashi T (1991) Debris flows. IAHR Monograph, A. A. Balkema: Rotterdam

Tecca P, Genevois R, Deganutti A, Armento MC (2007) Numerical modelling of two debris-flows in the Dolomites (Northeastern Italian Alps), Debris-flow Hazards Mitigation, Mechanics, Prediction, and Assessment, Chen CL, Major JJ (eds). Millpress, Rotterdam, pp 179–188

Volkwein A (2014) Flexible debris flow barriers. Design and application. WSL Berichte, 18. Birmensdorf, Swiss Federal Institute for Forest, Snow and Landscape Research WSL

Wendeler C, McArdell BW, Rickenmann D, Volkwein A, Roth A, Denk M (2006) Field testing and numerical modeling of flexible debris flow barriers. In Proceedings of the 6th international conference on physical modelling in geotechnics, Hong Kong, pp 1573–1578

White DJ, Take WA, Bolton MD (2003) Soil deformation measurement using particle image velocimetry (PIV) and photogrammetry. Géotechnique 53(7):619–631

Zanuttigh B, Lamberti A (2006) Experimental analysis of the impact of dry avalanches on structures and implication for debris flows. J Hydraul Res 44(4):522–534